International Journal of Modern Physics A
Vol. 36, Nos. 2 & 3 (2021) 2140020 (14 pages)

DOI: 10.1142/S0217751X21400200

World Scientific
www.worldscientific.com

Satellite architecture and preliminary in-orbit experiment of Taiji-1

Zhiming Cai[*,†] and Jianfeng Deng[*,‡]

On behalf of The Taiji Scientific Collaboration[†]

[*]*Innovation Academy for Microsatellites, Chinese Academy of Sciences, Shanghai, China*

[†]*Zhejiang University, Hangzhou, China*
[‡]*dengjf@microsate.com*

Received 15 September 2020
Revised 16 October 2020
Accepted 30 October 2020
Published

Taiji-1 is China's first in-orbit technology validating satellite related to spaceborne gravitational wave (GW) detection. The satellite was launched at 600km sun synchronized orbit on 31 August 2019. It has accomplished its mission goals while all subsystems have validated their key technologies in orbit. The subsystems include optical metrology system (OMS), drag-free attitude control system (DFACS), thermal control subsystem, high-quality microgravity satellite platform and so on. This paper presents system architecture of Taiji-1 analyzing in-orbit experimental results of thermal stability, reaction wheel vibration contributing to the noise of gravitational reference sensor (GRS) measurement noise, and the center-of-mass (CoM) of GRS calibration.

Keywords : Micro-vibration; mK thermal stability; CoM calibration; drag-free control; spaceborne gravitational wave detection.

1. Introduction

In early 2016, LIGO[1] published the results of directly detecting GW, verifying Einstein's prediction in General Relativity. According to the General Relativity, accelerating massive objects could generate gravitational waves that travel through the universe at the speed of light. The exciting news of LIGO stimulated the enthusiasm for GW detection and research, because GW will open a brand-new window for cosmology compared to electromagnetic waves.

Observing spaceborne GW is able to seek underlying universe governed by the gravitational interaction and explore the expanding gravitational universe and the nature of gravity beyond the General Relativity. With the GW event called GW170817 detected by advanced LIGO and Virgoobservatories,[2] the Hubble constant by a so-called standard siren method was firstly applied.[3] Reference 4 discussed that using spaceborne GW

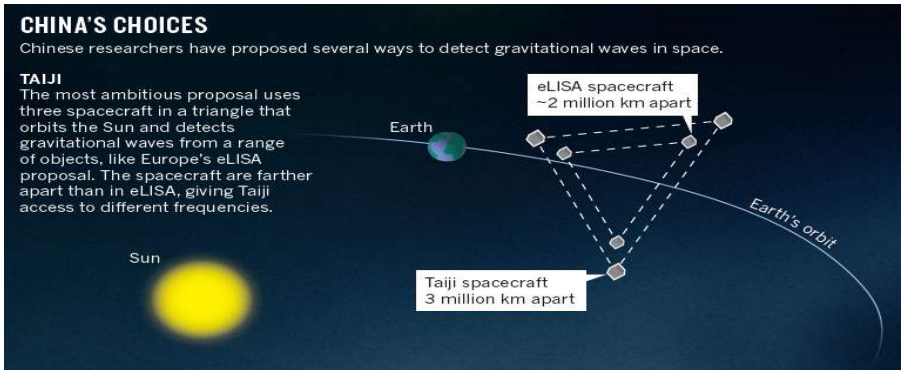

Fig. 1. The configuration of eLISA and Taiji.[6]

antenna could further improve the fractional uncertainty of Hubble constant determination.

Chinese Academy of Sciences (CAS) proposed a spaceborne GW observation program named "Taiji".[5] Compared to ground-based GW detection like LIGO, Taiji is designed with a lower detection frequency band. The sensitive frequency band of Taiji ranges from 0.1mHz to 1Hz, while the frequency bands of ground GW antenna are mostly concentrated in the range of 10Hz to 10kHz. It is obvious that a wide frequency band for GW observation could be built combining Taiji with ground GW antenna.

Taiji program is aimed at forming an equilateral triangle at geliocentric Earth trailing orbits, with three spacecrafts orbiting the sun. The three spacecrafts are 3×10^6 km apart from each other as shown in Fig. 1. Each spacecraft contains two test masses (TM), adopting DFACS in order to reduce the nonconservative force disturbance for the TMs free falling in inertial reference. The distance change between the two TMs through the laser interferometric ranging system. When the GW passes by, the optical path between the test masses will be changed. The change of optical path can be read out by the laser interferometry system so as to detect the GW signal.

Taiji's requirement to the strain sensitivity for GW detection is reduced to $10^{-20}/\sqrt{\text{Hz}}$. Even with the arm length of 3×10^6 km, it still requires TM's acceleration residual under $3\times10^{-15}\text{m/s}^2/\sqrt{\text{Hz}}$ and interferometry measurement noise under 8×10^{-12} m/$\sqrt{\text{Hz}}$. The requirements bring in great challenge to current technologies. In order to implement such precise mission, it is necessary to conduct in-orbit technology validation in an early phase. Taiji-1 aims to verify the key instruments and technologies that Taiji needs, such as OMS, DFACS, high stability thermal control technology and high-quality microgravity satellite platform.

The remainder of the paper is organized as follows: Section 2 illustrates the architecture of Taiji-1; Section 3 gives the primary in-orbit experiment results. The conclusion and future work are presented in Sec. 6.

2. Taiji-1 Architecture

2.1. *System architecture*

The block diagram of Taiji-1 is shown in Fig. 2. Top measurement requirement of OMS is within 100pm/√Hz and the DFACS is within 10^{-9}m/s^2/√Hz. The DFACS consists of GRS, drag-free controller, radio frequency ion μN thruster, Hall μN thruster. The OMS consists of the optical bench, phasemeter, two laser sources and OMS Front-End Electricity (FEE). To meet the requirements, Taiji-1 is designed with three-axis stabilized pointing strategy and a 600km circular dawn/dusk Sun-synchronous orbit with inclination of 97.69°. The orbit provides a relatively stable sun-facing angle, which guarantees energy supply and low thermal fluctuation on satellite shown in Fig. 3.

Satellite coordinate system (Os—XsYsZs) is defined as : +X axis points to satellite flying direction, +Z Axis points to earth center, *Z* Axis — The *X*-axis and the *y*-axis completes the right-handed system.

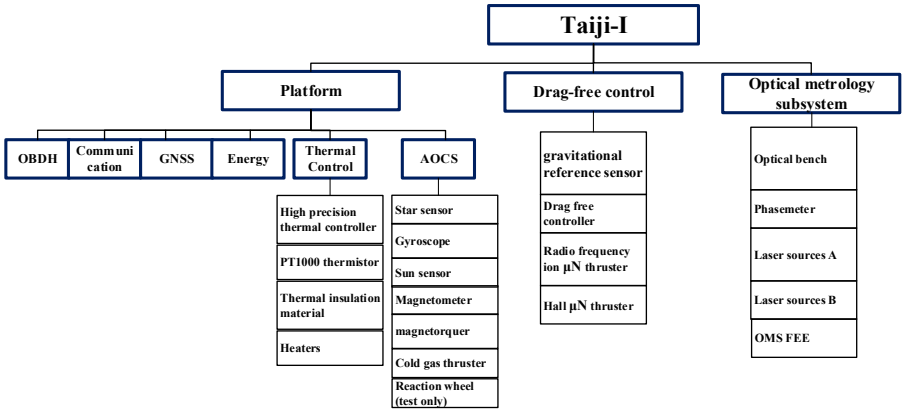

Fig. 2. The block diagram of Taiji-1 satellite.

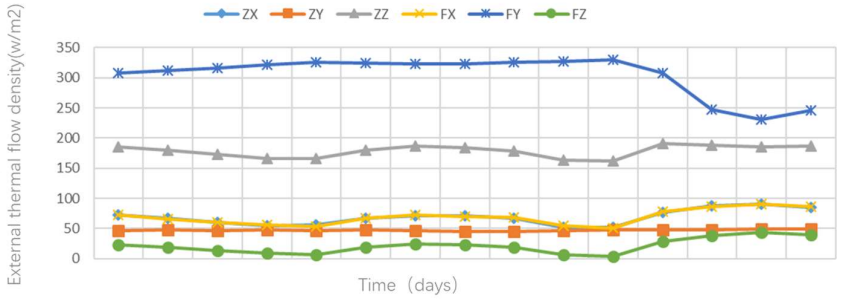

Fig. 3. Thermal flow density of the orbit.

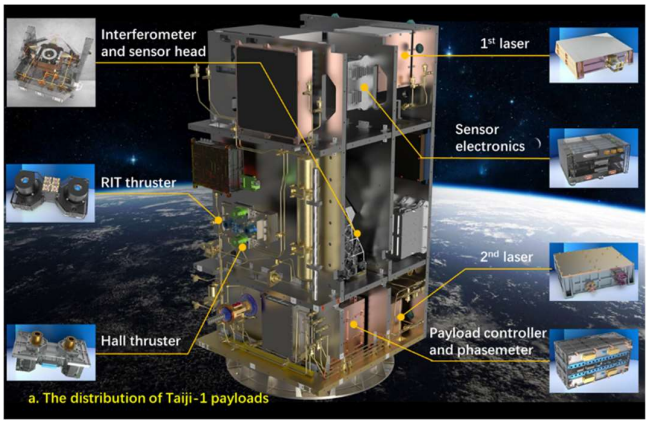

Fig. 4. The layout of the payload.

Fig. 5. The measurement of CoM of Taiji-1.

Figure 4 shows the main payloads layout in Taiji-1. Optical bench and TM are placed at the center of satellite. The distance between the COM of TM and the satellite is less than 0.1mm after mass compensation before launch as shown in Fig. 5. In-orbit COM evaluation will be illustrated in the next chapter. Thermal subsystem comprises thermal controller with 0.1mK thermal measurement resolution, PT1000 thermistor and heaters. Due to the constraint of micro gravity requirements to GRS payload, thermal subsystem radiation and conduction adopt multi-level thermal control method rather than heat pipes. The first level is satellite level control using active or passive thermal control, providing ~±1200mK thermal stability in satellite environment; Second level adopts close-loop active thermal control guaranteeig middle cabin of satellite (outside Optical bench and GRS TM) thermal fluctuation under ~±350mK; the last level using high insulation material and thermal flux isolation provides ~2.6mK thermal stability.

The attitude and orbit control subsystem (AOCS) comprise star tracker, gyroscopes, sun sensor, magnetometer, magnetorquer, cold gas thrusters and the controller. Considering the reliability of the satellite and micro-vibration test, a reaction wheel

(RW90-SP003 Reaction Wheel with Angular momentum 0.35 Nms) is installed along the *y*-direction of the satellite. The attitude sensors consist of star tracker, sun sensor, gyroscope and magnetometer. The star tracker and the gyroscope are used for attitude precision control, and the sun sensor and magnetometer are used for attitude capture and stabilization in the separation stage of the satellite and rocket.

2.2. *Mission model*

In order to validate the technical feasibility of Taiji-1, nine mission modes are designed. The mission modes at each stage and switching process are shown in Fig. 6.

Rate damping mode: The function of rate damping mode is to dampen the angular velocity deviation caused by the separation of the satellite and rocket to a smaller range ($\omega \le 0.014 rad/s$).

Attitude capture mode: The function of attitude acquisition mode is to realize the satellite's rapid ground orientation after rate damping.

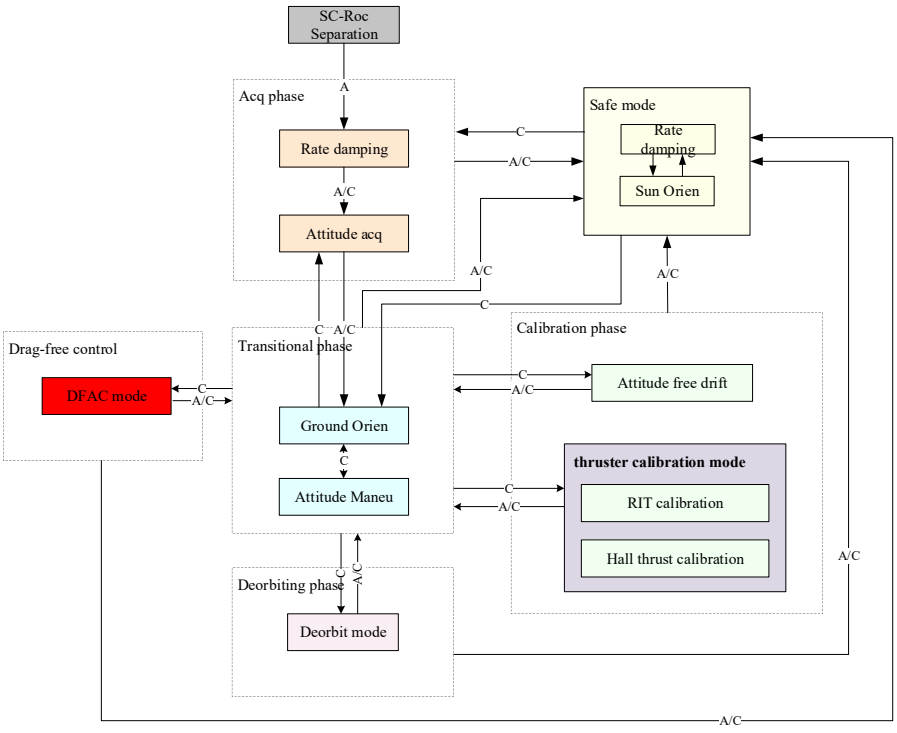

Fig. 6. The mission modes at each stage and switching process.

Ground orientation mode: The function of ground orientation mode is to stabilize the ground orientation. The star sensor is normally available to ensure stable satellite attitude.

Attitude free drift mode: The satellite attitude is not controlled, and the satellite attitude is free to drift under the influence of external environment interference. In this mode, the inertial sensor calibration works.

Electric micro thruster calibration mode: In this mode, the RIT and Hall effect thruster will be calibrated. The satellite automatically turns back to the ground orientation mode after calibration.

Drag-free control mode: The main mission mode of technology valibration, the acceleration and displacement mode DFAC experiment will be carried out. The satellite automatically returns to the ground orientation mode after drag-free control.

Attitude maneuver mode: The attitude maneuver mode is to realize the maneuver adjustment of any satellite attitude and provide the necessary attitude for calibration of the payload's relevant parameters.

Safe mode: Safe mode rate damping and safe mode orientation to Sun are included. The function of the safe mode is to adjust the satellite control to dampen the angular velocity of the satellite when a serious failure occurs on the satellite. After that, the satellite is controlled to achieve orientation to the sun in order to take in enough energy.

Deorbit mode: This mode is used for off-track operation at the end of satellite life.

3. Primary in-Orbit Experimental Results

The micro-vibration, thermal stability of the platform and the TM's CoM measurement experiment are illustrated and discussed in the chapter.

3.1. *Micro-vibration test*

In Ground orientation mode, the reaction wheel and the magnetorquer are used as the actuators for attitude control. An experiment was arranged to analyze reaction wheel inducing micro-vibration of the satellite platform. In this part, the effect of reaction wheel loading, unloading and normal working on the micro-vibration of satellite platform is analyzed.

During ground orientation mode, the rotating speed of reaction wheel is 100 *r*/s, while the unloading and loading speed are 2 *r*/s and 10 *r*/s, respectively. The magnetorquer and cold gas microthruster are used to unload the reaction wheel. The random shock disturbance would occur in the satellite platform due to the on-off of cold gas thrusters.

As shown in Figs. 7 and 8, the disturbance acceleration caused by the RW during loading and unloading phase is random, because the on-off of the electromagnetic valve could generate a shock on the satellite and GRS can sensor the vibration. During the normal ground orientation mode, the rotation speed of RW is constant with 100*r*/s, a

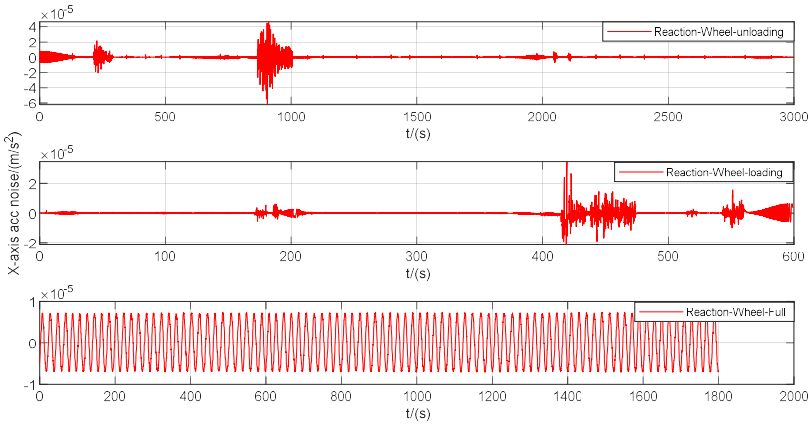

Fig. 7. The disturbance acceleration in *X*-axis caused by the RW time domain.

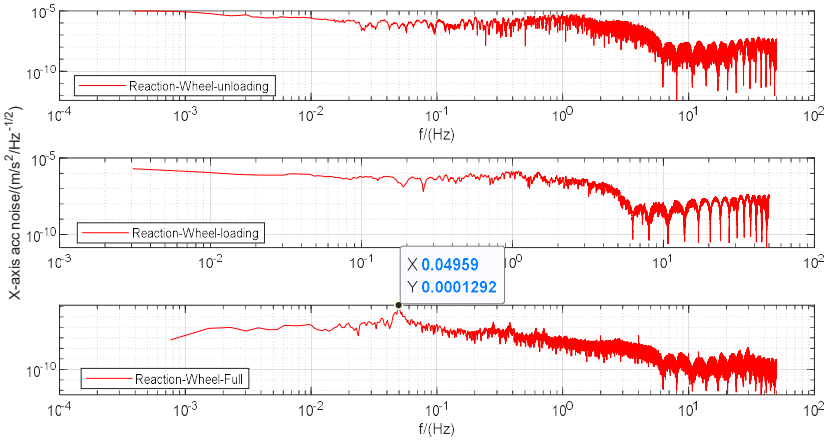

Fig. 8. The disturbance acceleration in *X*-axis caused by the RW in PSD.

sinusoidal regular vibration with the frequency about 0.05Hz and amplitude $2.54\times10^{-5}\,m/s^2$ is generated, and the reason is still under research. Based on the above analysis, the RW and the cold gas thruster should be shut off to provide a low micro-vibration satellite platform for the electric micro thruster calibration and DFC experiment.

3.2. *Thermal stability test result*

Thermal stability is an extremely critical element affecting the performance of the whole payload. This part analyzes in-orbit test result of the thermal control subsystem and its effect on the GRS noise.

Table 1. The performance of the thermal control subsystem for the payload.

Payloads	Laser A	Laser B	RF flow unit	Hall flow unit	Optical bench
Temperature (℃)	22.0000	22.0000	20.0162	19.9996	15.6819
	±0.0100	±0.1600	±0.1427	±0.0112	±0.0048

Table 2. The correlation of the temperature variance with GRS output.

序号	Free drift time	CW45 (℃)	CW46 (℃)	X1 ACC-Mean（V）	Y-ACC-Mean（V）	Z1 ACC-Mean（V）
1	20191108T22:08	1.85	6.04	0.14225	−0.07278	−0.07567
2	20191109T00:55	18.19	26.38	0.1446	−0.07018	−0.07279
3	20191109T08:13	19.96	27.93	0.14474	−0.06997	−0.07251
4	20191109T13:45	20.03	27.97	0.14473	−0.06994	−0.07253
5	20191109T17:59	20.00	28.08	0.1447	−0.06996	−0.07246
6	20191109T23:54	20.04	28.36	0.14472	−0.06989	−0.07245
7	20191110T06:35	20.01	28.16	0.14468	−0.0699	−0.07247
8	20191110T10:46	20.00	28.04	0.14465	−0.06993	−0.07246
9	20191111T00:06	20.06	28.4	0.14466	−0.06987	−0.07234
10	20191111T05:57	19.99	28.0	0.14461	−0.06991	−0.07247
11	20191111T09:14	19.95	27.93	0.1446	−0.06992	−0.07247
12	20191111T09:14	20.03	28.37	0.14462	−0.06984	−0.07242
13	20191112T04:31	19.98	27.94	0.14458	−0.06987	−0.07245
14	20191112T07:53	20.04	28.06	0.14458	−0.06986	−0.0724
15	20191112T22:52	20.08	28.45	0.14459	−0.0698	−0.07231
16	20191113T04:43	19.96	27.91	0.14454	−0.06985	−0.07243
17	20191113T08:05	20.06	28.09	0.14455	−0.06984	−0.07235
18	20191113T23:01	20.03	28.37	0.14457	−0.06977	−0.07233
19	20191114T08:15	20.00	27.99	0.14451	−0.06982	−0.07233
20	20191114T23:09	20.00	28.29	0.14453	−0.06976	−0.07225
21	20191115T08:29	20.02	28.04	0.1445	−0.06978	−0.07237
Correlation coefficient with CW46				0.987	0.9962	0.9957

As shown in Table 1, the thermal control subsystem can provide a relatively stable thermal environment for the payloads, especially for the optical bench, in which the sensitive head of the GRS and the interferometer requiring high thermal stability are installed. The change of the output of GRS with respect to the temperature and their correlation are shown in Table 2. The output of GRS and change of temperature at the temperature measurement point fixed on the surface of GRS FEE are shown in Figs. 9–11.

The symbols CW45 and CW46 represent the two temperature measurement points fixed on the surface of GRS FEE. The correlation coefficient of the GRS output with the temperature is calculated through the following equation

$$r_{T,GRS} = \frac{S_{T,GRS}}{S_T S_{GRS}} \tag{1}$$

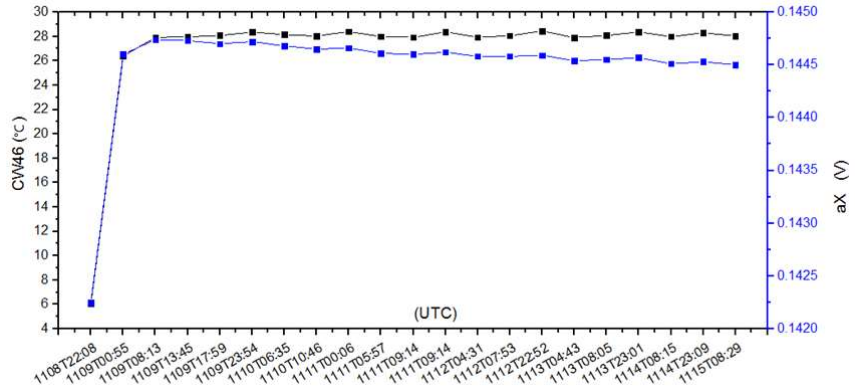

Fig. 9. The correlation of the output a_X with temperature.

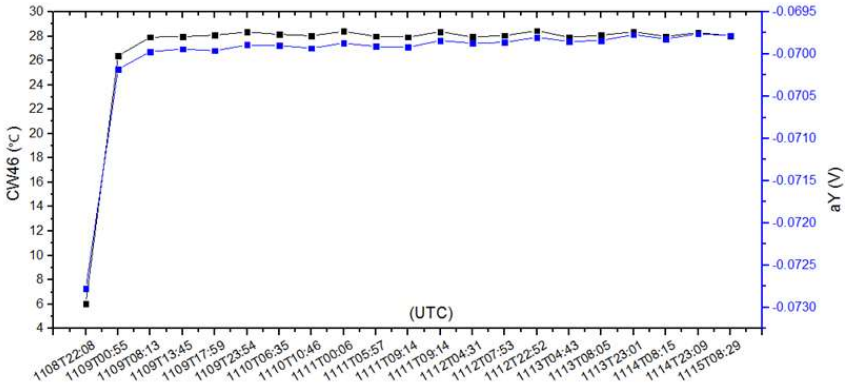

Fig. 10. The correlation of the output a_Y with temperature.

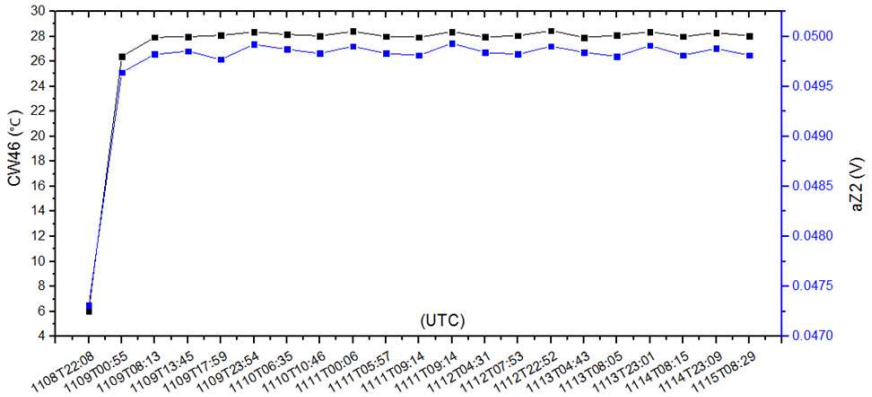

Fig. 11. The correlation of the output a_Z with temperature.

$S_{T,GRS}$ is the covariance of the temperature and the output voltage of GRS, S_T is the standard deviation of temperature, S_{GRS} is the standard deviation of GRS's output voltage. The value range of the correlation coefficient $r_{T,GRS}$ is [0,1], $r_{T,GRS}$=1 means that the two variables are completely linearly correlated, $r_{T,GRS}$=0 means that the two variables are not correlated. The closer the value is to 0, the weaker the correlation of the two variables.

From Table 2, it can be concluded that the temperature of GRS FEE stabilizes two days after the GRS is turned on, and the correlation coefficient of the output of GRS with the temperature is larger than 0.98 in the three axes. As shown in Figs. 8–10, the tendence of temperature and GRS output with time in the seven days experiments is almost the same, which also confirms their correlation. Through the thermal stability experiment, it is concluded that the temperature variance will have an impact on the GRS measurement. Thermal stability of GRS FEE is one of the key factors of GRS performance.

3.3. *CoM measurement result*

The relative distance between the CoM of the GRS and the satellite is an important factor influencing the measurement of the GRS when the satellite is during an attitude maneuvering mode. In this part, we describe the method and in-orbit experiment to estimate the relative position of the CoM of TM to the satellite.

The output acceleration of GRS expressed in the satellite body frame can be described as

$$\begin{aligned} \tilde{\boldsymbol{a}}_{body} &= \boldsymbol{T}_T^B \left(\boldsymbol{a}_{TM} + \boldsymbol{a}_{bias} + \boldsymbol{a}_n \right) \\ \boldsymbol{T}_T^B &= \begin{bmatrix} 0 & 0 & -1 \\ 0 & -1 & 0 \\ -1 & 0 & 0 \end{bmatrix} \end{aligned} . \tag{2}$$

Here, $\tilde{\boldsymbol{a}}_{TM}$ is the actual measured acceleration in the TM frame, $\boldsymbol{T}_T^B$ is the transformation matrix from TM to satellite body frame, and $\left(\boldsymbol{T}_B^T\right)^{-1} = \left(\boldsymbol{T}_B^T\right)^T = \boldsymbol{T}_T^B$, $\boldsymbol{a}_{bias}$ is the constant bias of the GRS, $\boldsymbol{a}_n$ is the measurement noise, which is supposed to be white noise.

The actual acceleration can be modeled as follows

$$\boldsymbol{a}_{TM} = \dot{\boldsymbol{\omega}}_{SC,I} \times \boldsymbol{r}_{TM,CoM} + 2\boldsymbol{\omega}_{SC,I} \times \dot{\boldsymbol{r}}_{TM,CoM} + \boldsymbol{\omega}_{SC,I} \times \left(\boldsymbol{\omega}_{SC,I} \times \boldsymbol{r}_{TM,CoM} \right) + \boldsymbol{a}_{SC,I} + \boldsymbol{g}_g , \tag{3}$$

$\tilde{\boldsymbol{a}}_{SC,I}$ is the nonconservative acceleration on satellite platforms, $\boldsymbol{\omega}_{SC,I}$, $\dot{\boldsymbol{\omega}}_{SC,I}$ are the angular velocity and angular acceleration of the satellite with respect to the inertial frame, $\boldsymbol{g}_g$ is the gravity gradient caused by the mass eccentricity of the satellite, $\boldsymbol{r}_{TM,CoM}$ is the relative position of the CoM of TM with respect to the CoM of the satellite, which is to be estimated. Typically, we suppose that $\boldsymbol{r}_{TM,CoM}$ will not change with time, Eq. (3) can be simplified to

$$\begin{aligned} \boldsymbol{a}_{TM} &= \boldsymbol{a}_{Manu} + \boldsymbol{a}_{SC,I} + \boldsymbol{g}_g = \dot{\boldsymbol{\omega}}_{SC,I} \times \boldsymbol{r}_{TM,CoM} + \boldsymbol{\omega}_{SC,I} \times \left(\boldsymbol{\omega}_{SC,I} \times \boldsymbol{r}_{TM,CoM} \right) + \boldsymbol{a}_{SC,I} + \boldsymbol{g}_g \\ \boldsymbol{a}_{Manu} &= \dot{\boldsymbol{\omega}}_{SC,I} \times \boldsymbol{r}_{TM,CoM} + \boldsymbol{\omega}_{SC,I} \times \left(\boldsymbol{\omega}_{SC,I} \times \boldsymbol{r}_{TM,CoM} \right) \end{aligned} . \tag{4}$$

Here, $\tilde{\boldsymbol{a}}_{Manu}$ represents the acceleration caused by the attitude maneuver of the satellite, and can be rewritten as

$$\tilde{\boldsymbol{a}}_{Manu} = \tilde{\boldsymbol{A}}\boldsymbol{r}_{TM,CoM} = \begin{bmatrix} -\omega_y^2-\omega_z^2 & \omega_x\omega_y-\dot{\omega}_z & \omega_x\omega_z+\dot{\omega}_y \\ \omega_x\omega_y+\dot{\omega}_z & -\omega_x^2-\omega_z^2 & \omega_y\omega_z-\dot{\omega}_x \\ \omega_x\omega_z-\dot{\omega}_y & \omega_z\omega_y+\dot{\omega}_x & -\omega_x^2-\omega_y^2 \end{bmatrix} \boldsymbol{r}_{TM,CoM}. \tag{5}$$

Here, $\boldsymbol{r}_{TM,CoM}=\begin{bmatrix} r_x & r_y & r_z \end{bmatrix}^T$, $\boldsymbol{\omega}_{SC,I}=\begin{bmatrix} \omega_x & \omega_y & \omega_z \end{bmatrix}^T$ and $\dot{\boldsymbol{\omega}}_{SC,I}=\begin{bmatrix} \dot{\omega}_x & \dot{\omega}_y & \dot{\omega}_z \end{bmatrix}^T$.

During the satellite attitude maneuver, the main input of GRS is the disturbance acceleration caused by satellite rotation.

In order to calibrate the mass eccentricity of the TM to the CoM of the satellite, an experiment is carried out as following:

Step 1. From time T0 to T1, an active torque is generated by the magnetic torque, spinning the satellite, the gyroscope and star tracker will measure the angular velocity and Euler angle of the satellite.

Step 2. Extracting the Euler angle and angular velocity from the star tracker and gyroscope respectively, receiving the effective signal after outlier removal, deviation correction, interpolation and downsampling filtering. A second-order polynomial fitting method is adopted to get the angular accelerations $\dot{\boldsymbol{\omega}}_{SC,I}$.

From Eq. (2), the change of the acceleration during attitude maneuvering can be modeled as

$$\begin{aligned} \Delta\tilde{\boldsymbol{a}}_{body,k} &= \tilde{\boldsymbol{a}}_{body,k} - \tilde{\boldsymbol{a}}_{body,k-1} \\ &= \boldsymbol{T}_B^I\left(\boldsymbol{a}_{TM,k}+\boldsymbol{a}_{bias,k}+\boldsymbol{a}_n-\boldsymbol{a}_{TM,k-1}+\boldsymbol{a}_{bias,k-1}+\boldsymbol{a}_{n,k-1}\right) \approx \boldsymbol{T}_B^I\left(\boldsymbol{a}_{TM,k}-\boldsymbol{a}_{TM,k-1}+\boldsymbol{a}_n\right). \end{aligned} \tag{6}$$

And the theoretical angular velocity and angular acceleration can be represented by the fitted value from Step 2. Combing Eqs. (4)–(6), a new measurement equation at time step k can be obtained

$$\boldsymbol{T}_B^T\Delta\tilde{\boldsymbol{a}}_{body,k}+\tilde{\boldsymbol{a}}_n=\tilde{\boldsymbol{a}}_{C,k}+\tilde{\boldsymbol{a}}_n=\begin{bmatrix} -\omega_{y,k}^2-\omega_{z,k}^2 & \omega_{x,k}\omega_{y,k}-\dot{\omega}_{z,k} & \omega_{x,k}\omega_{z,k}+\dot{\omega}_{y,k} \\ \omega_{x,k}\omega_{y,k}+\dot{\omega}_{z,k} & -\omega_{x,k}^2-\omega_{z,k}^2 & \omega_{y,k}\omega_{z,k}-\dot{\omega}_{x,k} \\ \omega_{x,k}\omega_{z,k}-\dot{\omega}_{y,k} & \omega_{z,k}\omega_{y,k}+\dot{\omega}_{x,k} & -\omega_{x,k}^2-\omega_{y,k}^2 \end{bmatrix}\boldsymbol{r}_{TM,CoM}. \tag{7}$$

The subscript k means time step k.

Three components are included in the measured acceleration $\tilde{\boldsymbol{a}}_{C,k}$; therefore, any component can be used to estimate the vector $\boldsymbol{r}_{TM,CoM}$. The component in the x_b-axis is adopted, which corresponds to the z-axis (the most sensitive axis) of the GRS, and the measurement equations are changed to

$$\tilde{\boldsymbol{y}}=\bar{\boldsymbol{A}}\boldsymbol{r}_{TM,CoM}+\boldsymbol{v}_n. \tag{8}$$

Here, $\tilde{\boldsymbol{y}}=\begin{bmatrix} a_{x,1} & a_{x,2} & \cdots & a_{x,n} \end{bmatrix}^T$ is the measurement sequence of the x-axis, $\bar{\boldsymbol{A}}$ is the reconstruction matrix described as follows

$$\bar{\boldsymbol{A}}=\begin{bmatrix} \left(\tilde{A}_{11}\right)_1 & \left(\tilde{A}_{12}\right)_1 & \left(\tilde{A}_{13}\right)_1 \\ \left(\tilde{A}_{11}\right)_2 & \left(\tilde{A}_{12}\right)_2 & \left(\tilde{A}_{13}\right)_2 \\ \vdots & \vdots & \vdots \\ \left(\tilde{A}_{11}\right)_n & \left(\tilde{A}_{12}\right)_n & \left(\tilde{A}_{13}\right)_n \end{bmatrix}. \tag{9}$$

And $\boldsymbol{cov}\left(\boldsymbol{v}_n\boldsymbol{v}_n^T\right)=\boldsymbol{R}_x$ is the measurement noise, the minimal variance estimator[7] of $\boldsymbol{r}_{TM,CoM}$ is shown as follows

$$\hat{\boldsymbol{r}}_{TM,CoM}=\left(\bar{\boldsymbol{A}}^T\boldsymbol{R}_x^{-1}\bar{\boldsymbol{A}}\right)^{-1}\bar{\boldsymbol{A}}\boldsymbol{R}_x^{-1}\tilde{\boldsymbol{y}}\,. \tag{10}$$

The results are shown as follows: Figs. 12 and 13 show the angular velocity and the fitted angular acceleration of the satellite during the maneuvering time.

As shown in Table 3, the best calibration accuracy of r_x is 0.02mm, while r_y is 0.04mm and r_z is 0.23mm. The identification accuracy of r_x and r_y is better than that of r_z, which is the reason that the noise resolution of GRS's y and z axis is one order better than x-axis. In addition, from the different maneuvering times, it is concluded that 1–3 min maneuvering time is acceptable. The accuracy of mass eccentricity will decrease when the maneuvering time is too long, because it is assumed that the nongravitational acceleration and gravity gradient remain unchanged during the maneuvering time. As the time increases, the accuracy of this assumption would be less, which is not conducive to the improvement of the accuracy of CoM eccentricity identification.

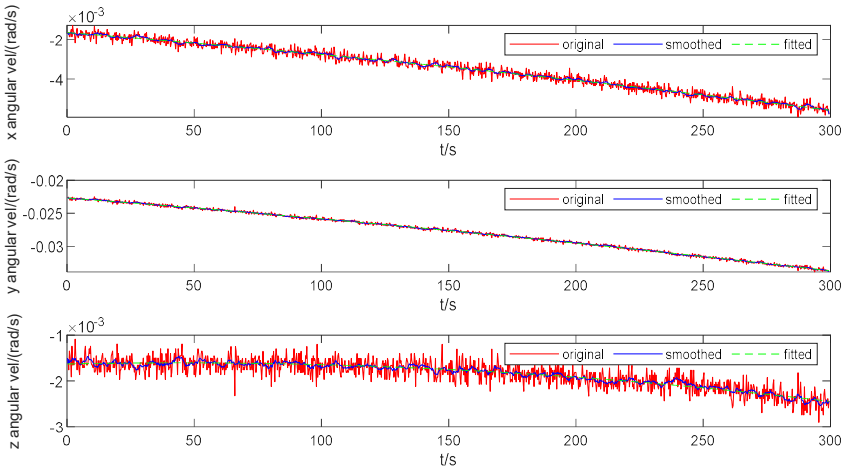

Fig. 12. The angular velocity of satellite.

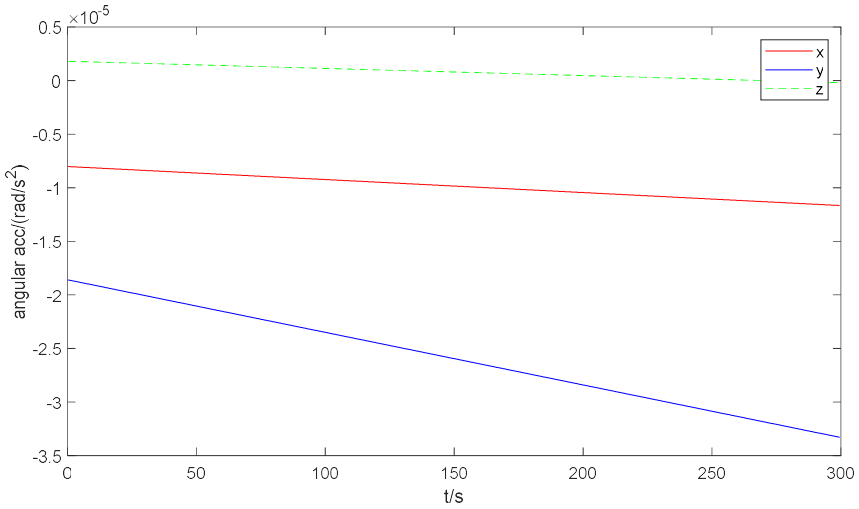

Fig. 13. The angular acceleration of the satellite.

Table 3. The CoM calibration error on-orbit.

Maneuvering Time	1 min	2 min	3 min	4 min	5 min
r_x (mm)	0.02	0.03	0.02	0.03	0.04
r_y (mm)	0.08	0.13	0.04	0.08	0.16
r_z (mm)	0.23	0.26	0.33	0.41	0.68

4. Conclusion

In the paper, we illustrate Taiji-1's architecture, mission modes and analyze in-orbit experiment results. The effect of the loading, unloading and normal work of RW on the vibration of the platform are analyzed and discussed. The thermal stability and its correlation with the measurement output of GRS are demonstrated and discussed. A special in-orbit experiment is designed and the minimal variance estimator is used to estimate the deviation of the CoM of TM to the satellite, and the estimation accuracy is better than 0.05mm. The relationship of the rotation speed of RW with the platform micro-vibration need to be confirmed and more in-orbit tests will be conducted in the near future.

Acknowledgments

This work is supported by the "Strategic Priority Research Program of the Chinese Academy of Science" (XDA15020705, XDA15020706, XDA15020707).

References

1. The LIGO Scientific Collaboration, *Class. Quant. Grav.* **32**, 074001 (2015).
2. The Virgo Scientific Collaboration, *Class. Quant. Grav.* **32**, 024001 (2015).
3. B. P. Abbott *et al*., *Nature* **551**, 85 (2017).
4. The Taiji Scientific Collaboration, *Commun. Phys.* (2020). (to be printed).
5. Taiji program white book (Inter report).
6. Z. R. Luo, Y. L. Wu *et al*., Gravitational wave detection and the nature of gravity, University of Chinese Academy of Sciences Report.
7. J. L. Crassidis, J. L. Junkins, *Optimal Estimation of Dynamic Systems* (CRC Press, 2011).

Please provide vol. no. and starting page for ref. 4.